Relative permeabilities and coupling effects in steady-state gas-liquid flow in porous media: A lattice Boltzmann study

Haibo Huang[a)] and Xi-yun Lu
Department of Modern Mechanics, University of Science and Technology of China, Hefei, Anhui 230026, China

(Received 1 May 2009; accepted 5 August 2009; published online 10 September 2009)

In this paper, the viscous coupling effects for immiscible two-phase (gas-liquid) flow in porous media were studied using the Shan–Chen-type single-component multiphase lattice Boltzmann model. Using the model, the two-phase flows in porous media with density ratio as high as 56 could be simulated and the contact angle of the gas-liquid interface at a solid wall is adjustable. To investigate viscous coupling effects, the co- and countercurrent steady-state two-phase flow patterns and relative permeabilities as a function of wetting saturation were obtained for different capillary numbers, wettabilities, and viscosity ratios. The cocurrent relative permeabilities seem usually larger than the countercurrent ones. The opposing drag-force effect and different pore-level saturation distributions in co- and countercurrent flows may contribute to this difference. It is found that for both co- and countercurrent flows, for strongly wet cases and viscosity ratio $M>1$, k_{nw} increase with the driving force and the viscosity ratio. However, for neutrally wet cases, the variations of k_{nw} and k_w are more complex. It is also observed that different initial pore-level saturation distributions may affect final steady-state distribution, and hence the relative permeabilities. Using the cocurrent and countercurrent steady flow experiments to determine the generalized relative permeabilities seems not correct. © *2009 American Institute of Physics*. [doi:10.1063/1.3225144]

I. INTRODUCTION

A. Two-phase flow in porous media

It is well known that the isotropic flow of a Newtonian fluid through a porous medium can be described by Darcy's law $\mathbf{u}=-k\mathbf{G}/\mu$, where $\mathbf{u}$ is the average velocity of the fluid in the direction of pressure gradient, $\mathbf{G}$ is the driving force per unit volume or pressure gradient, and μ is the viscosity of the fluid. The k is the permeability in the direction of the $\mathbf{G}$. It measures the ability of porous media to transmit fluids in a specified direction.

For multiphase flows in porous media, a typical situation is that the wetting phase covers the solid surface and moves along the surface, while the nonwetting phase flows in the center of the pores and surrounded by the wetting fluid. Hence, there is strong viscous coupling between the wetting and nonwetting fluids.[1] The viscous coupling effect means the momentum transfer between the two fluids.[2]

To account for viscous coupling effects, usually four dimensionless relative-permeability parameters k_{ij} are used to measure the effective permeability of two-phase flow. They are defined by modifying Darcy's law as in[3] $\mathbf{u}_i=-\Sigma_{j=1}^{2}(kk_{ij}\mathbf{G_j}/\mu_j)$, where i and j indicate phase 1 or 2 and $\mathbf{u}_i$ is the average velocity of fluid phase i. The relative permeabilities k_{ij} usually are functions of the wetting saturation S_w, capillary number Ca, and viscosity ratio M. S_w means the quantity of the wetting phase contained in a porous volume on a volumetric basis. $\mathrm{Ca}=u_w\mu_w/\sigma$ is the capillary number, where u_w is the average velocity of the wetting phase and σ is the surface tension. M is defined as $M=\mu_{\mathrm{nw}}/\mu_w$, which means the dynamic viscosity ratio between nonwetting and wetting fluids.

There are two possible ways to determine k_{ij} by performing two separate experiments. One way is applying the external force to each fluid separately, i.e., one experiment with $\mathbf{G}_1\neq 0$ and $\mathbf{G}_2=0$ and the other experiment with $\mathbf{G}_2\neq 0$ and $\mathbf{G}_1=0$. The second way is applying force to both fluids but one experiment with driving forces in the same direction, i.e., $\mathbf{G}_1=\mathbf{G}_2$ (cocurrent flow), and the other experiment with driving forces in the opposite direction, i.e., $\mathbf{G}_1=-\mathbf{G}_2$ (countercurrent flow). These two ways are all possible to give out four relevant permeabilities.[4]

In this paper we would focus on numerical study of the relative permeabilities in heterogeneous porous media. One of the most promising robust numerical methods on this study area is the lattice Boltzmann method (LBM).[1,4–8] LBM has been applied to study the oil-water displacement in porous media.[5–8] It has also been applied to study the low-density-ratio two-phase flow in homogeneous porous media;[4] it is found that the viscous coupling effect may be very different between the cocurrent and the countercurrent cases due to the pore-level saturation distribution. However, how the high-density-ratio gas-liquid flow relative permeabilities change with the wetting saturation S_w, capillary number Ca, and viscous ratio M in heterogeneous porous media has not yet been studied using LBM.

B. Lattice Boltzmann for multiphase flow

LBM is based on mesoscopic kinetic equations. Comparing with conventional methods for multiphase flows, LBM

[a)]URL: http://staff.ustc.edu.cn/~huanghb. Electronic mail: huanghb@ustc.edu.cn.

 © 2009 American Institute of Physics

Author complimentary copy. Redistribution subject to AIP license or copyright, see http://phf.aip.org/phf/copyright.jsp

does not track interfaces while sharp interfaces can be maintained automatically.[9] LBM has also been successfully applied to study wetting and spreading phenomena,[10–15] bubble collision and bubble rising phenomena,[9,16] etc.

There are several popular multiphase models in LBM. The first type is the color-gradient-based LBM proposed by Gunstensen *et al.*[17] which is based on the Rothman–Keller lattice gas model.[18] The second type is the original Shan–Chen (SC) model.[19] The third type is the free-energy-based LBM.[20] The last one is proposed by He *et al.*[21] which uses the idea of a level set.

Although LBM has made great progress in multiphase flow modeling, all the above LBMs are limited to small density ratios less than 10 because numerical instability may appear in cases of large density ratio. Inamuro *et al.*[9] and Lee and Lin[22] achieved a high density ratio through improving Swift's free-energy model[20] and the model of He *et al.*,[21] respectively. However, both of their models used two sets of particle distribution functions (PDFs) which undermines the simplicity of the LBM or increases computational loads. Recently, it is found that through using just one set of PDFs, different equations of state (EOSs) can be incorporated into the SC LBM so as to achieve a high density ratio.[23] The surface tension for different EOSs in SC LBM is able to be determined analytically.[12,24]

Yiotis *et al.* applied the multiphase model of He *et al.*[21] to study the immiscible two-phase flow in porous media and obtained some results.[1] However, in the model of He *et al.*,[21] two sets of PDFs were used and the surface tension has to be obtained through finite difference method. In addition to that, a special treatment may be necessary to handle the solid walls. Pan *et al.*[6] and Li *et al.*[7] applied SC two-component multiphase LBM to study the two-component flow in porous media. However, when using the SC two-component multiphase LBM, the viscosity ratio M is around 1 due to numerical instability and the maximum M in their study is only about 3.

As mentioned above, the revised single-component multiphase SC LBM (Ref. 23) can incorporate different EOSs into the model and high-density-ratio two-phase flow can be achieved. On the other hand, the wettability at solid-fluid interfaces about this model was fully studied by Benzi *et al.*[12] and different contact angles of the fluid-fluid interface at a solid wall can be obtained by adjusting the "density of wall" conveniently.[12] Here, we will focus on the SC LBM exclusively.

In this paper, the single-component multiphase SC LBM will be applied to study the high-density-ratio two-phase flow in heterogeneous porous media. We first briefly review the SC single-component multiphase LBM. Then SC LBM code was validated by verifying the velocity profile and relative permeabilities for a layered two-phase flow through a two-dimensional (2D) channel. After that, the multiphase flow in porous media with different capillary numbers, wettabilities, and viscosity ratios was simulated and analyzed.

II. METHOD

A. Shan-and-Chen-type single-component multiphase LBM

Here we implement the SC LBM (Ref. 19) in two dimensions for a single-component multiphase system. In the model, one distribution function is introduced for the fluid. The distribution function satisfies the following lattice Boltzmann equation:

$$f_a(\mathbf{x}+\mathbf{e}_a\Delta t, t+\Delta t) = f_a(\mathbf{x},t) - \frac{\Delta t}{\tau}[f_a(\mathbf{x},t) - f_a^{\mathrm{eq}}(\mathbf{x},t)], \quad (1)$$

where $f_a(\mathbf{x},t)$ is the density distribution function in the ath velocity direction and τ is a relaxation time which is related to the kinematic viscosity as $\nu = c_s^2(\tau - 0.5\Delta t)$. The equilibrium distribution function $f_a^{\mathrm{eq}}(\mathbf{x},t)$ can be calculated as

$$f_a^{\mathrm{eq}}(\mathbf{x},t) = w_a\rho\left[1 + \frac{\mathbf{e}_a\cdot\mathbf{u}^{\mathrm{eq}}}{c_s^2} + \frac{(\mathbf{e}_a\cdot\mathbf{u}^{\mathrm{eq}})^2}{2c_s^4} - \frac{(\mathbf{u}^{\mathrm{eq}})^2}{2c_s^2}\right]. \quad (2)$$

In Eqs. (1) and (2), the $\mathbf{e}_a$ are the discrete velocities. For the D2Q9 model, they are given by

$$[\mathbf{e}_0,\mathbf{e}_1,\mathbf{e}_2,\mathbf{e}_3,\mathbf{e}_4,\mathbf{e}_5,\mathbf{e}_6,\mathbf{e}_7,\mathbf{e}_8] = c\begin{bmatrix} 0 & 1 & 0 & -1 & 0 & 1 & -1 & -1 & 1 \\ 0 & 0 & 1 & 0 & -1 & 1 & 1 & -1 & -1 \end{bmatrix}.$$

In Eq. (2), for the D2Q9 model, $w_a = 4/9$ $(a=0)$, $w_a = 1/9$, $(a=1,2,3,4)$, $w_a = 1/36$, $(a=5,6,7,8)$, and $c_s = c/\sqrt{3}$, where $c = \Delta x/\Delta t$ is the ratio of lattice spacing Δx and time step Δt. Here, we define one lattice unit (Δx) as 1 lu and one time step (Δt) as 1 ts. In Eq. (2), ρ is the density of the fluid, which can be obtained from $\rho = \Sigma_a f_a$.

In the SC LBM, the effect of body force is incorporated through adding an acceleration into the velocity field. The macroscopic velocity $\mathbf{u}^{\mathrm{eq}}$ is given by

$$\mathbf{u}^{\mathrm{eq}} = \mathbf{u}' + \frac{\tau\mathbf{F}}{\rho}, \quad (3)$$

where $\mathbf{u}'$ is the velocity defined as

$$\mathbf{u}' = \frac{\Sigma_a f_a \mathbf{e}_a}{\rho}. \quad (4)$$

In Eq. (3), $\mathbf{F} = \mathbf{F}_{\mathrm{int}} + \mathbf{F}_{\mathrm{ads}} + \mathbf{G}$ is the force acting on the fluid, here including the interparticle force $\mathbf{F}_{\mathrm{int}}$, adhesion force between liquid/gas phase and solid phase, $\mathbf{F}_{\mathrm{ads}}$, and an external force $\mathbf{G}$. In this study $\mathbf{G}$ is a steady body force. The actual whole fluid velocity $\mathbf{u}$ is defined as[10]

$$\mathbf{u} = \mathbf{u}' + \frac{\mathbf{F}}{2\rho}, \quad (5)$$

which means the "fluid velocity" should be calculated correctly by averaging the momentum before and after the collision.[10] The interparticle force is defined as[5]

$$\mathbf{F}_{\mathrm{int}}(\mathbf{x},t) = -g\psi(\mathbf{x},t)\sum_a w_a\psi(\mathbf{x}+\mathbf{e}_a\Delta t,t)\mathbf{e}_a, \quad (6)$$

where g is a parameter that controls the strength of the interparticle force. For the EOS proposed by Shan and Chen,[19]

Author complimentary copy. Redistribution subject to AIP license or copyright, see http://phf.aip.org/phf/copyright.jsp

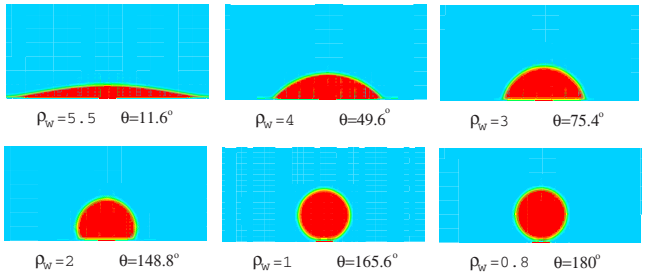

FIG. 1. (Color online) Different contact angles obtained through adjusting the parameter ρ_w. RK EOS was used in the simulations.

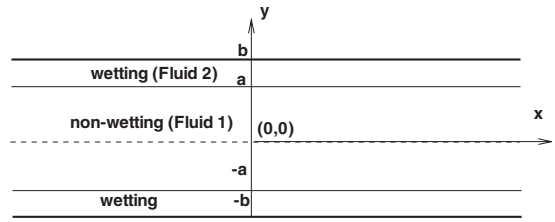

FIG. 2. Cocurrent immiscible two-phase flow in a 2D channel. The wetting (fluid 2) phase flows along the upper and lower plates while nonwetting phase (fluid 1) flows in the center region.

$$\psi(\rho) = \rho_0[1 - \exp(-\rho/\rho_0)], \tag{7}$$

where ψ is an effective number density[19] and ρ_0 is a constant.

Through Taylor expanding as described in Appendix A in Ref. 24 and $-\partial_j p + \partial_i(c_s^2\rho) = F_i$ (here i and j means the x or y coordinates), we obtained the pressure p as[24]

$$p = c_s^2\rho + \frac{c_s^2 g}{2}\psi^2. \tag{8}$$

According to Yuan and Schaefer,[23] if the EOS of $p = p(\rho)$ is already known, we can use the following formula:

$$\psi = \sqrt{\frac{2(p - c_s^2\rho)}{c_s^2 g}}, \tag{9}$$

to incorporate different EOSs into the SC LBM.

The typical EOSs are the van der Waals, Redlich–Kwong (RK), Redlich–Kwong–Soave, Peng–Robinson, and Carnahan–Starling (CS) equations. They are given out in detail in Ref. 23. The surface tension was calculated through Laplace law after the equilibrium state obtained in LBM simulations. Analytical solutions of surface tension for these EOSs can also be conveniently obtained through solving equations in Ref. 24.

The desired contact angle can also be obtained conveniently through changing parameter ρ_w.[12] The adhesion force between gas/liquid phase and solid walls is calculated by Eq. (10); here we assume the density of solid phase is ρ_w, i.e., $\psi[\rho(x_w)] = \psi(\rho_w)$,

$$\mathbf{F}_{\text{ads}}(\mathbf{x},t) = -g\psi[\rho(\mathbf{x},t)]\sum_a w_a\psi(\rho_w)s(\mathbf{x}+\mathbf{e}_a\Delta t,t)\mathbf{e}_a. \tag{10}$$

Here $s(\mathbf{x}+\mathbf{e}_a\Delta t,t)$ is an indicator function that is equal to 1 or 0 for a solid or a fluid domain node, respectively. ρ_w is not really relevant to the "true" density of the solid phase; it is a free parameter used here to tune different wall properties.[12]

In our simulations, any lattice node in the computational domain represents either a solid node or a fluid node. For the solid node, before the streaming step, the bounce-back algorithm instead of the collision step is implemented to mimic nonslip wall boundary condition.

Figure 1 demonstrates that different contact angles can be obtained through adjusting ρ_w. In these simulations, the computational domain is 200×100, the upper and lower boundaries are solid walls, and the east and west boundaries are periodic. The EOS used in the LB simulation is the RK EOS:

$$p = \frac{\rho RT}{1 - b\rho} - \frac{a\rho^2}{\sqrt{T}(1 + b\rho)}, \tag{11}$$

with $a=\frac{2}{49}$, $b=\frac{2}{21}$, $T_c=0.1961$, and $T=0.85T_c$. The liquid phase density is $\rho_l=6.06$ and gas phase density is $\rho_g=0.5$. When the parameter ρ_w varies between ρ_l and ρ_g, the contact angle varies between 0° and 180°. The surface tension σ in the above case is about 0.16 in the numerical simulation and the value of surface tension is adjustable through changing parameter b in the EOS.

When using the SC LBM, it is found that there are spurious velocities near curved interfaces and the magnitude of the spurious velocities becomes larger when the density ratio increases.[23] It has been found that highly isotropic gradient operators are able to reduce the spurious velocities.[25] Here for simplicity, the highly isotropic gradient operators were not adopted in our LBM code. The spurious velocities near curved interfaces do have a minor effect on the two-phase flow-flux calculation at the inlet and outlet boundaries. The flow-flux calculation should exclude these spurious velocities near curved interfaces.

III. RESULTS AND DISCUSSION

A. Viscous coupling in cocurrent flow in a 2D channel

For immiscible two-phase flows in porous media, a typical situation is that the wetting fluid attaches and moves along the solid surface, while the nonwetting phase flows in the center of the pores. The velocity of the nonwetting phase is relevant to the viscosity ratio of the nonwetting and wetting fluids, i.e., $M=\frac{\mu_{\text{nw}}}{\mu_w}$.

Here we studied the immiscible two-phase cocurrent flow through two parallel plates. In the simulation, the periodic boundary condition was applied in the inlet/outlet boundary. Nonslip (bounce-back) boundary conditions were applied in the upper and lower plates. The kinematic viscosity for nonwetting and wetting fluids is identical, i.e., $\nu_{\text{nw}} = \nu_w = c_s^2(\tau - 0.5)$, Hence $M = \rho_{\text{nw}}/\rho_w$.

In the simulation, as illustrated in Fig. 2, the wetting phase flows in the region $a<|y|<b$ and the nonwetting phase flows in the central region $0<|y|<a$. Obviously, the saturation of the wetting fluid in this study is $S_w = 1 - a/b$,

Author complimentary copy. Redistribution subject to AIP license or copyright, see http://phf.aip.org/phf/copyright.jsp

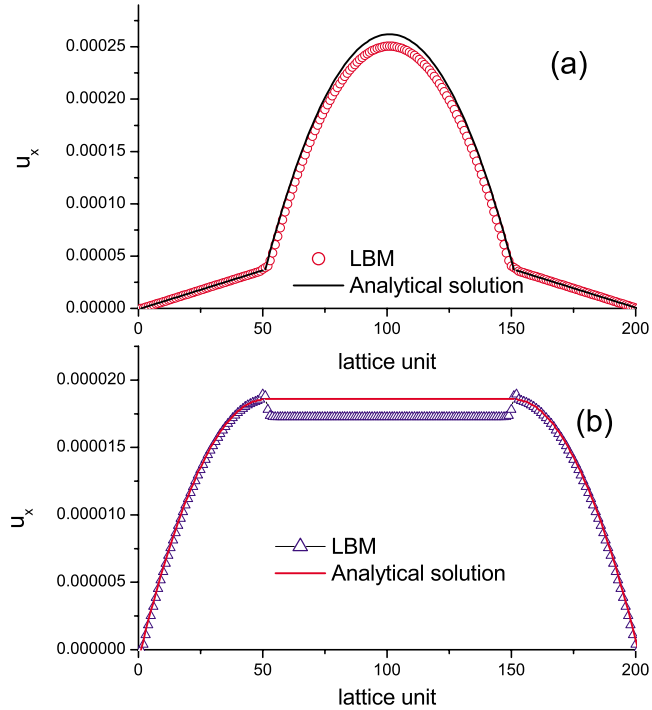

FIG. 3. (Color online) Velocity profile u_x in the middle of the 2D channel. The wetting phase is more viscous. $G=1.5\times10^{-8}$ was applied only on (a) fluid 1 and (b) fluid 2, $\tau=1.0$, $\nu=0.1667$, and $M=\frac{1}{12}$. The velocity profiles in (a) can be used to calculate the permeabilities k_{11} and k_{21} while those in (b) are used to calculate the permeabilities k_{12} and k_{22}.

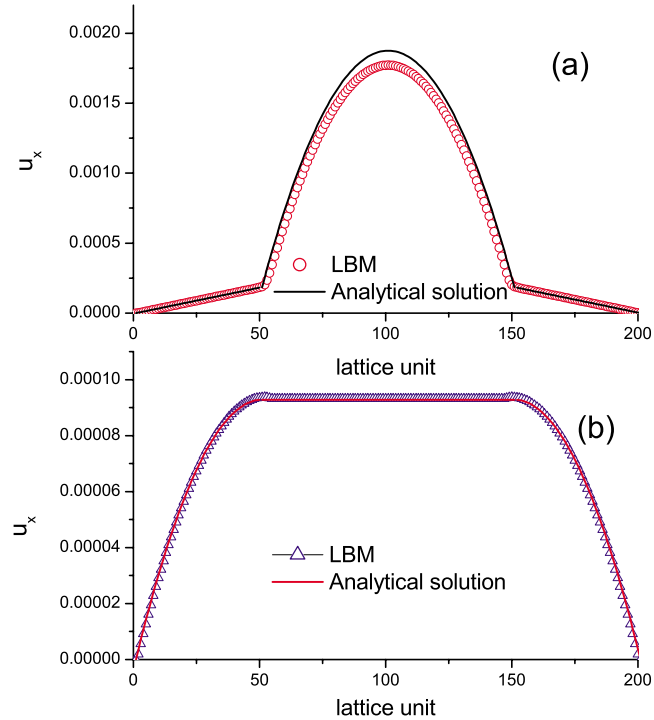

FIG. 4. (Color online) Velocity profile u_x in the middle of the 2D channel. The wetting phase is more viscous, $M=\frac{1}{18}$, $\tau=0.6$, and $\nu=0.0333$. $G=1.5\times10^{-8}$ was applied only on (a) fluid 1 and (b) fluid 2.

and $S_{\mathrm{nw}}=a/b$. Assuming a Poiseuille-type flow in the channel, the analytical solution for the velocity profile between the parallel plates is given in the Appendix.

From the analytical solution for the velocity profile and the definitions, the four relative permeabilities as a function of the nonwetting saturation can be obtained as

$$k_{11}=\frac{Q_1(G_2=0)}{Q_{10}}=S_{\mathrm{nw}}^3+3MS_{\mathrm{nw}}^2-3MS_{\mathrm{nw}}^3,$$

$$k_{21}=\frac{Q_2(G_2=0)}{Q_{10}}=\frac{3}{2}MS_{\mathrm{nw}}(1-S_{\mathrm{nw}})^2,$$

$$k_{12}=\frac{Q_1(G_1=0)}{Q_{20}}=\frac{3}{2}S_{\mathrm{nw}}(1-S_{\mathrm{nw}})^2, \tag{12}$$

$$k_{22}=\frac{Q_2(G_1=0)}{Q_{20}}=(1-S_{\mathrm{nw}})^3.$$

From Eq. (12), we can see that the $k_{i,2}\in[0,1]$ when saturation $S_w\in[0,1]$, while the $k_{i,1}$ may be higher than 1 when saturation $S_w\in[0,1]$ because $k_{i,1}$ is not only a function of S_w but also of M.

For the cases $M<1$, Fig. 3 shows the velocity profile for $M=\frac{1}{12}$ and $S_w=0.5$. In the figure, velocity profiles in (a) and (b) are obtained through applying body force $G=1.5\times10^{-8}$ only on fluid 1 and fluid 2, respectively. The mesh used in the simulation is 100×200. The velocity profile calculated from LBM agrees well with the analytical one. For the profile in (b), the nonwetting-phase velocity obtained from LBM is about 7% lower than that of the analytical one and there is a very small velocity jump near the interface.

The 7% discrepancy may be originally from the surface tension value. When $\tau=1$, the numerical surface tension is a little bit larger than the analytical one. The surface tension calculated with $\tau=0.6$ is found to be almost identical as the analytical one.[24] The SC LBM simulation using $\tau=0.6$ is also found to be able to give a very accurate velocity profile compared with the analytical solutions as shown in Fig. 4.

Although numerical simulation with $\tau=0.6$ is slightly more accurate than that with $\tau=1$, the numerical solution with $\tau=1$ is also acceptable because the discrepancy is very small. The more important issue is that in the LBM simulations, calculation with $\tau=1$ requires much less central processing unit (CPU) time (around 30% CPU time of the same case with $\tau=0.6$) to converge to a steady-flow state.

The profiles in (a) and (b) can be used to calculate the permeabilities k_{11} and k_{21} and k_{12} and k_{22}, respectively. Figure 5 illustrates the $k_{i,j}$ as a function of the S_w when $M<1$. Again, the LBM results agree well with the analytical curves. As expected in Eq. (12), relative permeabilities of both phases are smaller than 1.

For the cases $M>1$, Fig. 6 shows the velocity profile for $M=12$ and $S_w=0.5$. In the figure, velocity profiles in (a) and (b) are obtained through applying body force $G=1.5\times10^{-8}$ only on fluid 1 and fluid 2, respectively. The velocity profile obtained from LBM also agrees well with the analytical one. The profiles in (a) and (b) can be used to calculate the permeabilities k_{11} and k_{21} and k_{12} and k_{22}, respectively. Figure 7 illustrates the $k_{i,j}$ as a function of the S_w when $M>1$. The LBM result is very consistent with the analytical solution.

Author complimentary copy. Redistribution subject to AIP license or copyright, see http://phf.aip.org/phf/copyright.jsp

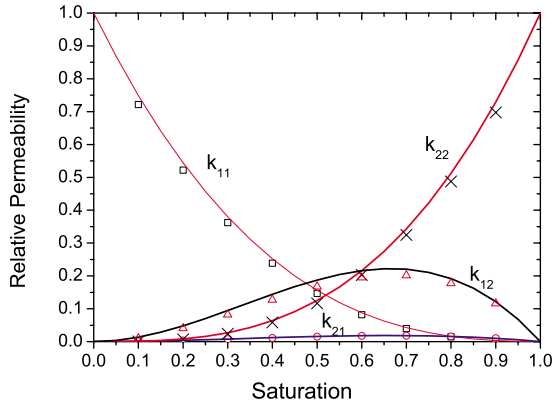

FIG. 5. (Color online) Relative permeabilities (k_{ij}) as a function of wet saturation for two-phase flow in a 2D channel. $M=\frac{1}{12}$.

From the figure, we can see that the k_{11} and k_{21} are greater than unity for most S_w values. That means the wetting and nonwetting phase flow fluxes are larger than the 100% nonwetting-saturated case for most S_w values if the driving force only acts on fluid 1. That is due to the "lubricating" effect of the wetting fluid.

B. Two-phase flow through porous media

In this section, two-phase flow in a porous medium is simulated. Porous medium structure generations are not a topic we are concerned with here. The porous medium in our simulations is the same as that in Ref. 1, which is represented by 2D pore networks of 20^2 lu^2 square solid and void (pore space) blocks. The porosity of the network is $\epsilon=0.77$. The size of the whole network is 400×400 lu^2.

Initially, the wetting and nonwettings phase were distributed randomly in the pores, i.e., wetting or nonwetting phases in each void blocks such that the desired wetting saturation was obtained. As we know, the specific randomization at the initial state may affect the phase distribution and hence the relative permeabilities.[7] In our C++ code, for each void block, (double)rand( )/(double)RAND_MAX$<S_w$ was used to initiate a case with specified S_w. Here except for the study on effect of initial phase distribution (Sec. III B 4), for a certain saturation in our simulations, the specific randomization is identical.

In the simulations, periodic boundary conditions were applied in all directions. Cocurrent and countercurrent flows were simulated by adding body forces G for both phases along the flow direction because adding body phase is simple and is able to avoid capillary pressure gradients and thus saturation gradients along the flow direction.[7] The wetting and nonwetting phase flow fluxes were calculated at the inlet and outlet during the simulations. If the relative flow-flux difference between every 4000 steps is less than 0.5%, it is assumed that the final steady state arrived.

In the simulations it is found that smaller droplet/bubbles may disappear. However, the mass of liquid or gas in the whole computational domain remains constant because the bigger droplet/bubbles grow at the same time. In that way, the flow system seems able to minimize the interfacial energy.[26] Hence actually this study investigates the liquid-vapor flow in porous media. The S_w and flow fluxes of the nonwetting and wetting phases in the outlet as a function of time step in a typical case are illustrated in Fig. 8. It is found that the variation of S_w is very small which means the vapor mass is conserved. At 56 000 ts, the above flow-flux criteria are satisfied and hence the final steady state is reached.

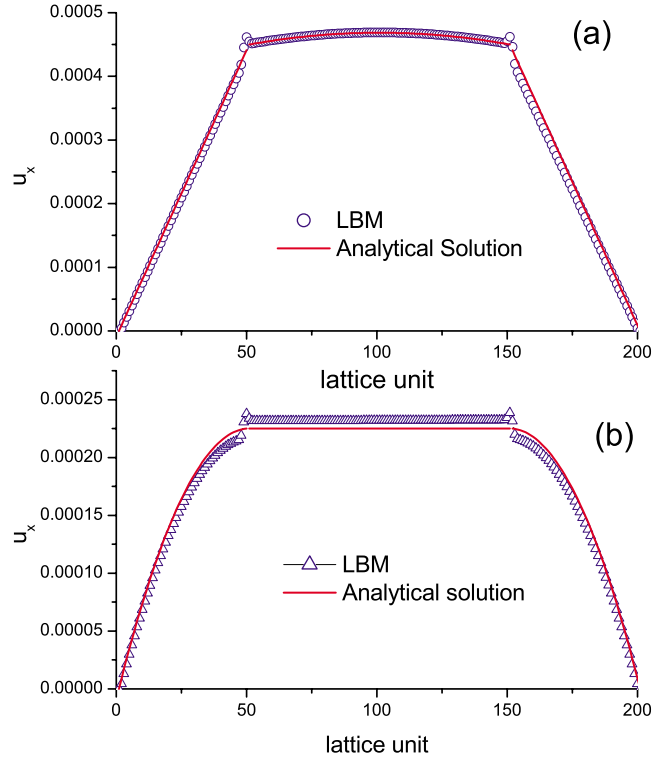

FIG. 6. (Color online) Velocity profile u_x in the middle of the 2D channel. The wetting phase is less viscous. $G=1.5\times10^{-8}$ was applied only on (a) fluid 1 and (b) fluid 2, $\nu=0.1667$, and $M=12$. The velocity profiles in (a) can be used to calculate the permeabilities k_{11} and k_{21} while those in (b) are used to calculate the permeabilities k_{12} and k_{22}.

It is well known that three nondimensional parameters are important for the immiscible two-phase flow through porous media. These parameters are viscosity ratio M, Reynolds number $\mathrm{Re}=ud/\nu$, and capillary number Ca. The d is the width of the smallest channel in porous media.

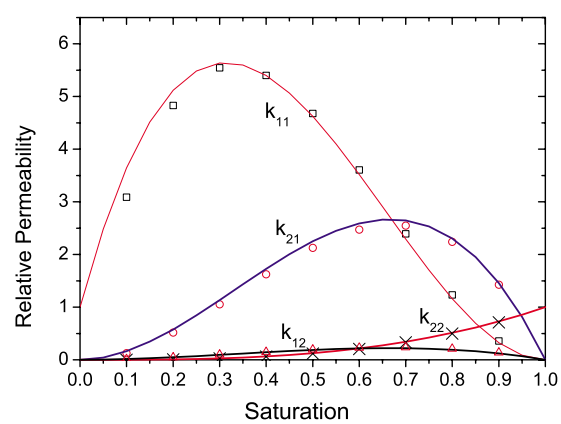

FIG. 7. (Color online) Relative permeabilities (k_{ij}) as a function of wetting saturation for two-phase flow in a 2D channel. $M=12$.

Author complimentary copy. Redistribution subject to AIP license or copyright, see http://phf.aip.org/phf/copyright.jsp

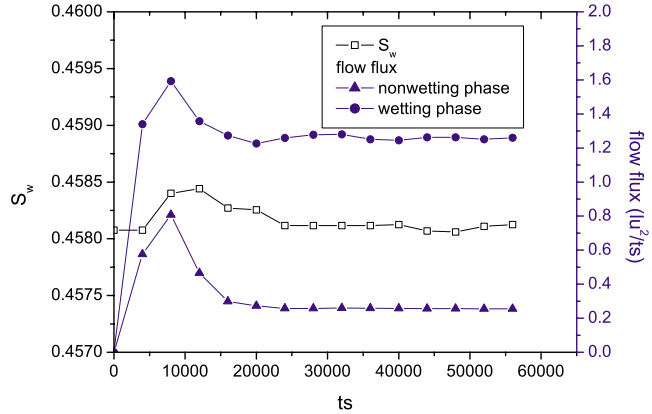

FIG. 8. (Color online) The S_w and flow fluxes in the outlet (bottom boundary) as a function of time step in a typical cocurrent-flow case with $S_w=0.45$ and $M=56$.

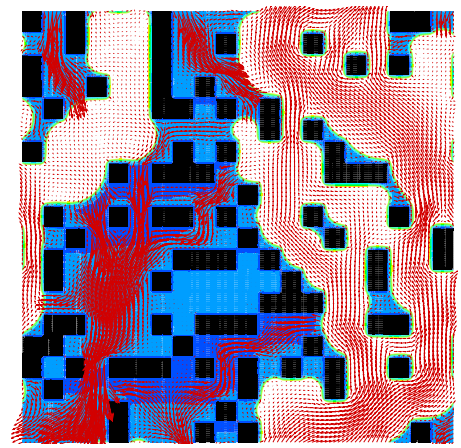

FIG. 10. (Color online) Velocity field for steady-state countercurrent two-phase flow in a 2D porous with $S_w=0.5$ and $G=10^{-4}$. The nonwetting phase is shown in white. RK EOS was applied in the LB simulation, $\sigma=0.16$, $M=12$, and $\theta=180°$.

In all of our simulations, the kinematic viscosity is $\nu=\frac{1}{3}(\tau-0.5)=0.1667$. The maximum gas velocity in our simulations was about $u=0.2$ lu/ts in the porosity 2D pore networks in 100% gas-saturated flow. The maximum Reynolds number in our simulations was $\mathrm{Re}=u\times 20/\nu=24$. Here we assumed that Darcy's law is valid in all of the cases we studied.

The capillary number Ca can be regarded as the ratio of the body forces to the interfacial forces.[1] In the following simulations, when using the RK EOS, $M=12$ and the applied body force in our simulations was $G=10^{-5}$ or $G=10^{-4}$. The corresponding capillary numbers are $\mathrm{Ca}=G/\sigma=10^{-5}/0.16=6.25\times 10^{-5}$ and 6.25×10^{-4}, respectively. These are relatively high-Ca cases, where the movement of the interface is mainly controlled by viscous forces.[1]

Figure 9 shows the initial and steady two-phase distribution patterns in the cases of $S_w=0.2$, $S_w=0.5$, and $S_w=0.8$ when $G=10^{-5}$. The upper and lower rows represent the initial and final steady-state two-phase distributions, respectively. They are strong wetting cases because $\rho_w=0.5$ and $\theta=180°$. In the figure, the wetting phase is shown in white.

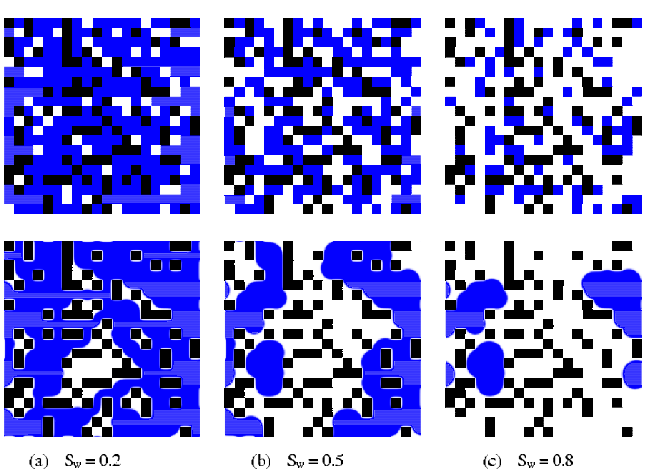

FIG. 9. (Color online) The cocurrent-flow initial (upper row) and final steady-state (lower row) two-phase distribution patterns in the cases of [column (a)] $S_w=0.2$, [column (b)] $S_w=0.5$, and [column (c)] $S_w=0.8$ when $G=10^{-5}$. In the LBM simulation, RK EOS was used, $\sigma=0.16$, $M=12$, and $\theta=180°$. The wetting phase is shown in white. The nonwetting phase is shown in dark gray and the solid is black.

Figure 9 shows that when $S_w=0.2$, the wetting phase is discontinuous and covers the solid surface, while the nonwetting phase is continuous and flows through the porous media. The wetting phase is practically immobile and $k_w=0$. The cocurrent k_{nw} is about 1.3 because nonwetting phase flows among the wetting phase films and takes advantage of the lubricating effect.

When $S_w=0.5$, the nonwetting and wetting phases are all continuous. For the case of $S_w=0.8$, as demonstrated in Fig. 9(c), the nonwetting phase forms several large blobs and is discontinuous. These blobs are trapped in big pores due to the resistance of capillary force and are immobile.

Figure 10 shows the velocity field of the case $G=10^{-4}$, $S_w=0.5$, and $M=12$ countercurrent steady flow. From the figure, we can see that usually the velocity magnitude in the nonwetting area is much smaller than that in the wetting area because the density of the nonwetting phase is high while the driving force G's magnitude is the same. Because the driving forces applied to the two phases are in opposite directions, the flows of the two phases are also in opposite directions.

Through integration of the velocity of each phase in the upper (inlet) and lower (outlet) boundaries, the permeabilities of each phase can be obtained. The co- and countercurrent-flow relative permeabilities k_{nw} and k_w as a function of S_w are shown in Fig. 11. The relative permeabilities of co- and countercurrent flows are all found to be convex functions of saturation. Due to the lubricating effect, the co- and countercurrent k_{nw} are larger than unity when $S_w<0.25$ for the cases of $G=10^{-5}$. The cocurrent permeabilities k_{nw} and k_w are found to be higher than the corresponding countercurrent ones. The opposing drag-force effect may contribute to the difference;[4] another possible reason is that the co- and countercurrent cases may make the pore-level saturation distribution different, and hence the viscous coupling and relative permeabilities.

Author complimentary copy. Redistribution subject to AIP license or copyright, see http://phf.aip.org/phf/copyright.jsp

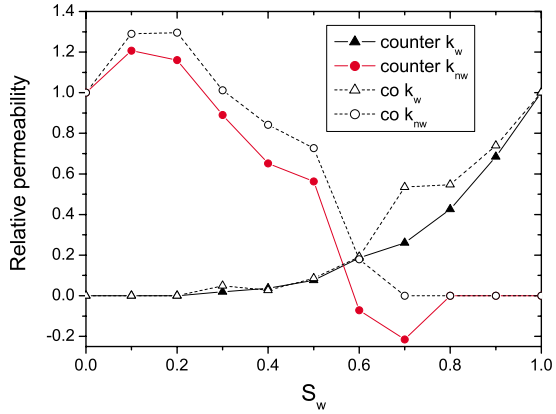

FIG. 11. (Color online) Relative permeabilities k_w and k_{nw} as a function of wetting saturation for cocurrent and countercurrent two-phase flows in a 2D porous. RK EOS was applied in the LB simulation, $\sigma=0.16$, $M=12$, $\theta=180°$, and $G=10^{-5}$.

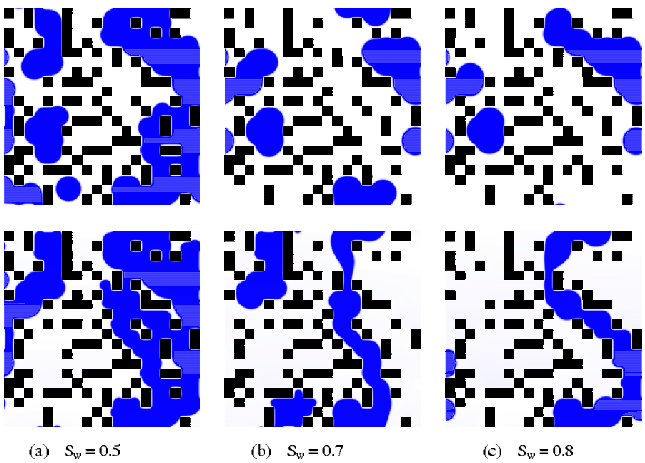

FIG. 12. (Color online) Countercurrent steady-state two-phase distribution patterns in the cases of [column (a)] $S_w=0.5$, [column (b)] $S_w=0.7$, and [column (c)] $S_w=0.8$ when $G=10^{-5}$ (upper row) and $G=10^{-4}$ (lower row). In the LBM simulation, RK EOS was used, $\sigma=0.16$, $M=12$, and $\theta=180°$. The wetting phase is shown in white. The nonwetting phase is shown in dark gray and the solid is black.

1. Effect of driving force (capillary number)

To discuss the effect of driving force on the relative permeabilities, cases of the co- and countercurrent flows with different driving forces are simulated. The countercurrent two-phase distribution patterns are shown in Fig. 12. The upper and lower rows show the cases of $G=10^{-5}$ and $G=10^{-4}$, respectively. The force applied to wetting and nonwetting phases is downward and upward, respectively. From the figure we can see that for these cases, increasing force may make the phase distribution change. For cases of $S_w=0.7$ and $S_w=0.8$, when $G=10^{-5}$ the nonwetting phase is discontinuous and mainly stays in large pores. However, when $G=10^{-4}$ the situation changes and the nonwetting phase is continuous and the nonwetting fluid can travel in the connected channel. For the case of $S_w=0.5$, increasing force also makes the disconnected nonwetting phase move but not remain static in large pores.

The above changes make the relative permeabilities change prominently. Figure 13 illustrate such changes. In the figure, for countercurrent flow (b), most k_{nw} of $G=10^{-4}$ are larger than those of $G=10^{-5}$ and the k_w changes little. The same phenomena were also observed in the cocurrent flows (a). Here, comparing (a) and (b) in the figure, again it is found that the cocurrent permeabilities k_{nw} and k_w are higher than the corresponding countercurrent ones.

Figure 14 shows the co- and countercurrent relative permeabilities k_w and k_{nw} as a function of driving force when $S_w=0.5$. For strongly wet cases (a), the co- and countercurrent k_{nw} increase and k_w changes little with the driving force. A possible reason is that when driving force increases, the nonwetting blobs in large pores tend to move and occupy more path to be connected; that would increase the k_{nw}.

However, for the neutrally wet cases in Fig. 14(b), the variations of k_{nw} and k_w are more complex. We will discuss the effect of wettability in Sec. III B 2.

2. Effect of wettability

In this section, the dependence of the relative permeability on wettability was studied. Neutrally wet cases were also simulated in our study. In the simulations, $\rho_w=2.2$ was used

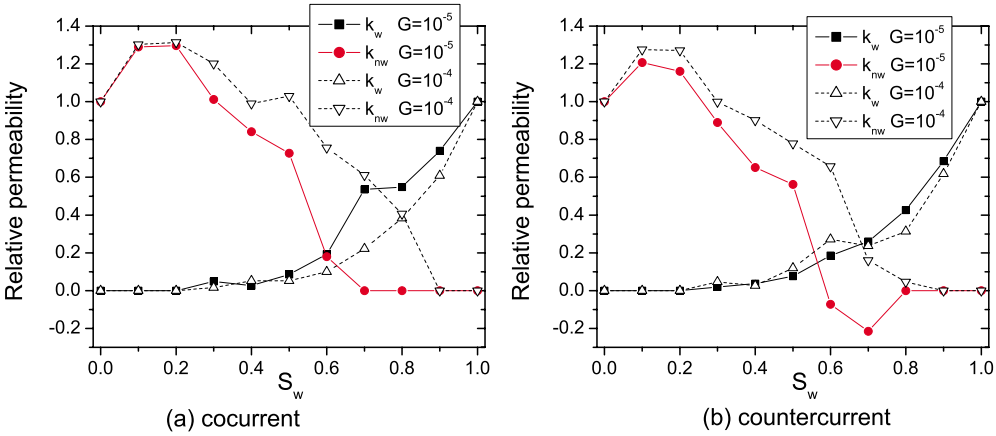

FIG. 13. (Color online) (a) Cocurrent and (b) countercurrent relative permeabilities k_w and k_{nw} as a function of wetting saturation when applied forces $G=10^{-4}$ and $G=10^{-5}$. RK EOS was applied in the LB simulation, $\sigma=0.16$, $M=12$, and $\theta=180°$.

Author complimentary copy. Redistribution subject to AIP license or copyright, see http://phf.aip.org/phf/copyright.jsp

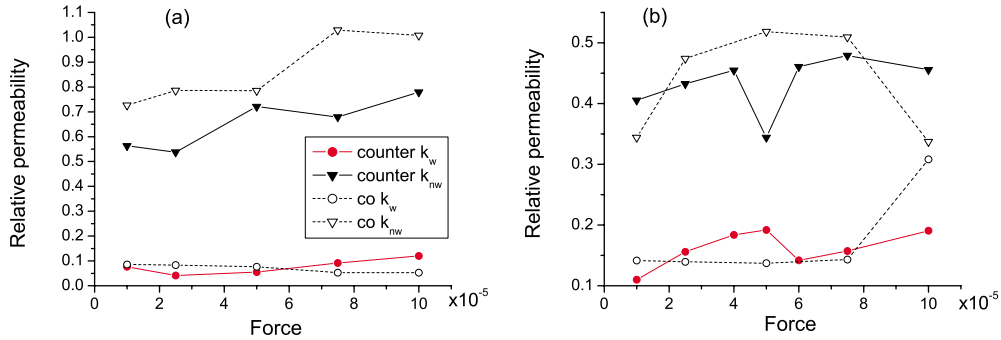

FIG. 14. (Color online) Co- and countercurrent relative permeabilities k_w and k_{nw} as a function of driving force (S_w=0.5). (a) strongly wet cases θ=180°; (b) neutrally wetting cases θ=103°. RK EOS was applied in the LB simulation. σ=0.16 and M=12.

to mimic the neutrally wet media; the corresponding contact angle for the more viscous phase is 103°. The driving force in simulations is $G=10^{-5}$.

In the neutrally wet porous media, cocurrent steady-state two-phase distribution patterns for different S_w are illustrated in Fig. 15. Comparing Figs. 9(c) and 15(c), it is observed that for S_w=0.8, the nonwetting phase has a smaller specific interfacial area with the solid phase, which means smaller resistance to flow, in the strongly wet media than in these neutrally wet media. For the other given S_w, the mechanism is also valid.[7] This mechanism seems dominant because it is found that the k_{nw} in the strongly wet media are higher than in the neutrally wet system when comparing Figs. 16 and 11.

Figure 16 shows the cocurrent and countercurrent relative permeabilities as a function of S_w. It seems that the cocurrent k_{nw} and k_w are all slightly larger than the countercurrent ones for most S_w.

Comparing Figs. 11 and 16, it is found that there is a very small difference for neutrally wet and strongly wet systems in terms of k_w. As we know, at a given saturation level, the nonwetting phase tends to occupy larger pores in strongly wet media, so the wetting phase tends to occupy a smaller pore space in the strongly wet media. This mechanism may make the k_w lower in strongly wet media than in the neutrally wet media. On the other hand, the wetting phase seems more connected in strongly wet media, which may make the k_w higher in strongly wet media.[7] Figure 16 demonstrates that the net effect of these two offsetting mechanisms is a relatively small difference in k_w as a function of S_w. The above results are consistent with the results of Li *et al.*[7]

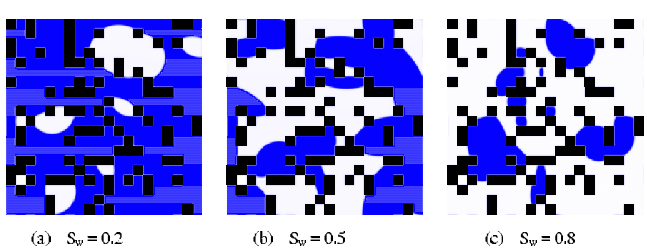

FIG. 15. (Color online) Steady-state cocurrent two-phase distribution patterns in the cases of S_w=0.2, S_w=0.5, and S_w=0.8 when Ca=6.25×10^{-5}. M=12, RK EOS was applied in the LB simulation, σ=0.16, ρ_w=2.2, and θ=103°. The wetting phase is shown in white and solid surface is black.

It is also found in Fig. 16 that the variations of k_{nw} and k_w as a function of S_w are not so smooth. Figure 14(b) also demonstrates the complex variations for neutrally wet cases. As we know for strongly wet cases, the nonwetting phase tends to be trapped into large pores and the wetting phase prefers attaching to solids. Hence the two-phase distribution is mainly determined by the pore structure of the porous media and driving forces. However, for neutrally wet cases, the phase distribution becomes more random than strongly wet cases because in neutrally wet cases, pore structure has less effect on the distribution of the two phases. As results would show in Sec. III B 4, different phase distributions would result in quite different k_{nw} and k_w. Hence, more random phase distribution may make the variations of k_{nw} and k_w more complex than strongly wet cases.

3. Effect of viscosity ratio

Here we focus on the topic about how relative permeabilities depend on the viscosity ratio M of two phases. In this section, the capillary number is set as Ca=6.25×10^{-5} for all simulations.

To achieve a higher density ratio, here in our LB simulations, the EOS used is the CS EOS:

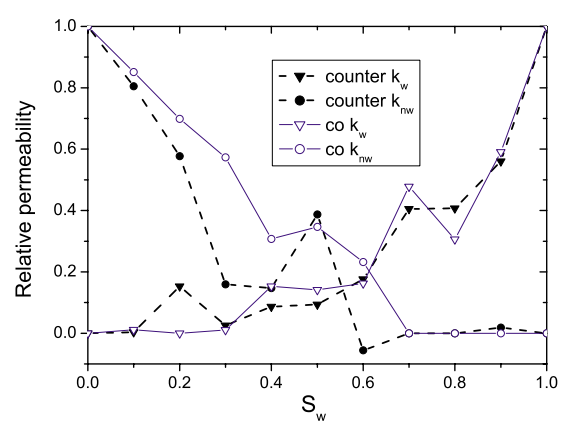

FIG. 16. (Color online) Cocurrent and countercurrent relative permeabilities k_w and k_{nw} as a function of wetting saturation for two-phase flow in a 2D porous. M=12, RK EOS was applied in the LB simulation, σ=0.16, ρ_w=2.2, and θ=103°.

Author complimentary copy. Redistribution subject to AIP license or copyright, see http://phf.aip.org/phf/copyright.jsp

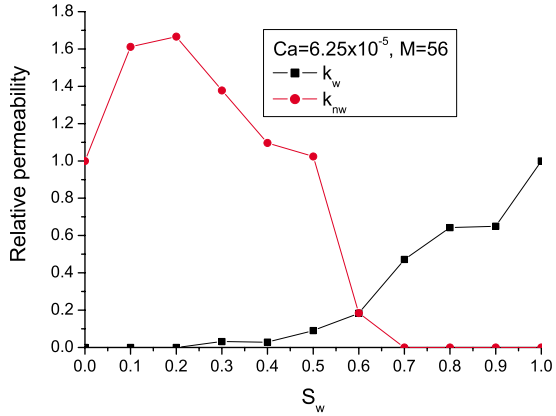

FIG. 17. (Color online) Relative permeabilities k_w and k_{nw} as a function of wetting saturation for cocurrent two-phase flow in a 2D porous. The CS EOS was used in the simulations, $\rho_{liquid}=0.359$, $\rho_{gas}=0.006\,45$, $\sigma=0.0145$, $M=56$, $Ca=6.25\times10^{-5}$, $G=9.06\times10^{-7}$, and $\theta=180°$.

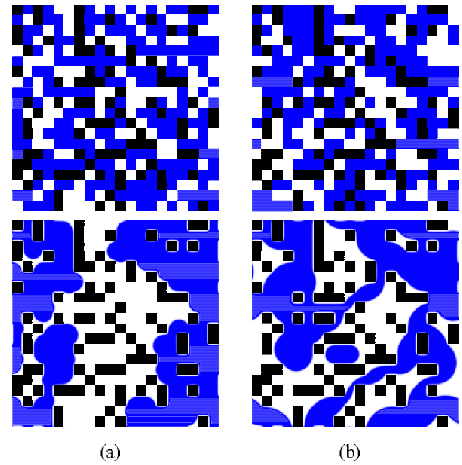

FIG. 18. (Color online) The cocurrent-flow initial (upper row) and final steady-state (lower row) two-phase distribution patterns for cases of $S_w=0.4$ and $G=10^{-5}$. Case (a) (left column) and case (b) (right column) have different initial phase distributions. In the LBM simulation, RK EOS was used, $\sigma=0.16$, $M=12$, and $\theta=180°$. The wetting phase is shown in white.

$$p=\rho RT\frac{1+b\rho/4+(b\rho/4)^2-(b\rho/4)^3}{(1-b\rho/4)^3}-a\rho^2,$$

with $a=1$, $b=4$, $T_c=0.0943$, and $T=0.7T_c$, the liquid phase density is $\rho_l=0.359$, and the gas phase density is $\rho_g=0.006\,45$. When the parameter ρ_w varies between ρ_l and ρ_g, the contact angle varies between 0° and 180°. Here all the cases are gas-wetting cases with $\rho_w=0.006\,45$.

Figure 17 shows the relative permeabilities as a function of S_w for $M=56$. Compared with Fig. 11, it is found that although Ca is the same, increase in M makes k_{nw} increase significantly, especially when the S_w is in the intermediate range. That is due to the lubricating effect of the wetting phase film which attaches the wall. It also demonstrates that the greater the viscosity ratio M, the larger the lubricating effect. It is also found that in cases of a higher M, there is more connected nonwetting phase pathway,[7,27] which may also contribute to the trend of k_{nw} increasing with M. On the other hand, the k_w is not so sensitive to M. That can be observed clearly in Figs. 11 and 17.

4. Effect of initial wetting-saturation distribution

The initial wetting-saturation distribution may affect the permeabilities. The cocurrent-flow initial (upper row) and final steady-state (lower row) two-phase distribution patterns for the case of $S_w=0.4$ and $G=10^{-5}$ are illustrated in Fig. 18.

In the figure, cases (a) and (b) have the same initial wetting saturation but different initial phase distributions. The final steady-state k_w of (a) and (b) are 0.027 and 0.034, respectively. k_{nw} are 0.842 and 0.522, respectively. Hence, different initial pore-level saturation distributions may result in different final phase distributions due to the complex heterogeneous porous structure and the driving force. That would affect the coupling effect and hence the relative permeabilities. Hence all the results in this paper also depend on the initial two-phase distributions.

IV. CONCLUSIONS

Our study demonstrates that SC single-component multiphase LBM is a very good tool to study the immiscible two-phase flow in porous media due to its simplicity and capability of investigating wettability effect and achieving high-density-ratio two-phase flow.

In this paper, the immiscible single-component two-phase flow in porous media was studied using the SC-type multiphase LBM. Co- and countercurrent two-phase distribution patterns and relative-permeability curves as a function of S_w for different wettabilities and viscosity ratios were obtained. When $M>1$, the k_{nw} may be greater than unity due to the lubricating effect, while when $M<1$, the k_{nw} and k_w are always less than 1.

The cocurrent k_{nw} and k_w seems usually larger than the countercurrent ones. Besides the opposing drag-force effect, the different pore-level saturation distributions in co- and countercurrent flows and hence the viscous coupling may also contribute to this discrepancy. It is found that for both co- and countercurrent flows, for strongly wet cases and $M>1$, k_{nw} increase with the driving force and the viscosity ratio M. For neutrally wet cases, the variations of k_{nw} and k_w are more complex. Different initial pore-level saturation distributions may affect the final steady- state distribution, and hence the relative permeabilities. Because pore-level saturation distribution and hence the k_{nw} and k_w may be very different in co- and countercurrent steady flow experiments, using the co- and countercurrent steady flow experiments to determine the generalized relative permeabilities seems not correct.

ACKNOWLEDGMENTS

This work was supported by the National Science Foundation of China (NSFC) (Grant No. 10802085) and the Innovation Project of the Chinese Academy of Sciences (Grant No. KJCX1-YW-21).

Author complimentary copy. Redistribution subject to AIP license or copyright, see http://phf.aip.org/phf/copyright.jsp

APPENDIX: ANALYTICAL SOLUTION FOR THE LAYERED MULTIPHASE FLOW IN A CHANNEL

Here the analytical solution for the velocity profile of the layered two-phase flow in a channel is given. The flow is illustrated in Fig. 2. In the figure, the wetting (phase 2) phase flows along the upper and lower plates while the nonwetting phase (phase 1) flows in the center. When the constant body forces G_1 and G_2 were applied to phase 1 and phase 2, respectively, the fluid flow of each phase was governed by the following equations:

$$\rho_1\nu_1\nabla^2 u_1 = G_1, \quad \rho_2\nu_2\nabla^2 u_2 = G_2,$$

where $u_1(y)$ and $u_2(y)$ are the velocities of phase 1 and phase 2, respectively. The boundary conditions are

$$(\partial_y u_1)|_{y=0} = 0, \quad \rho_1\nu_1(\partial_y u_1)|_{y=a} = \rho_2\nu_2(\partial_y u_2)|_{y=a},$$

$$u_1|_{y=a} = u_2|_{y=a}, \quad u_2|_{y=b} = 0.$$

Solving the above equations with the boundary conditions, we obtained the analytical solutions

$$u_1 = A_1 y^2 + C_1, \quad u_2 = A_2 y^2 + B_2 y + C_2,$$

where

$$A_1 = -\frac{G_1}{2\rho_1\nu_1}, \quad A_2 = -\frac{G_2}{2\rho_2\nu_2},$$

$$B_2 = -2A_2 a + 2MA_1 a,$$

$$C_1 = (A_2 - A_1)a^2 - B_2(b-a) - A_2 b^2,$$

$$C_2 = -A_2 b^2 - B_2 b,$$

and $M = \mu_1/\mu_2$ is the viscosity ratio.

With the above solutions, it is easy to get the relative permeabilities as illustrated in Eq. (12). The following is an example of how to get k_{11} in Eq. (12). As we know the volumetric flow rate for steady single-phase Darcy flow is

$$Q_{10} = \int_0^b (A_1 y^2 - A_1 b^2)dy = -\frac{2}{3}b^3 A_1,$$

and the phase 1 volumetric flow rate in the layered two-phase flow is

$$\begin{aligned} Q_1(G_2=0) &= \int_0^a u_1 dy \\ &= \int_0^a [A_1 y^2 - A_1 a^2 - 2MA_1 a(b-a)]dy \\ &= -\frac{2}{3}A_1 a^3 - 2MA_1 a^2 b + 2MA_1 a^3, \end{aligned}$$

where only G_1 applied to phase 1 and $G_2=0$. Hence, the k_{11} is

$$k_{11} = \frac{Q_1(G_2=0)}{Q_{10}} = S_{\mathrm{nw}}^3 + 3MS_{\mathrm{nw}}^2 - 3MS_{\mathrm{nw}}^3.$$

The other relative permeabilities in Eq. (12) can also be obtained.

[1] A. G. Yiotis, J. Psihogios, M. E. Kainourgiakis, A. Papaioannou, and A. K. Stubos, "A lattice Boltzmann study of viscous coupling effects in immiscible two-phase flow in porous media," Colloids Surf., A **300**, 35 (2007).
[2] O. R. Ayodele, "Theoretical analysis of viscous coupling in two-phase flow through porous media," Transp. Porous Media **64**, 171 (2006).
[3] F. Kalaydjian, "Origin and quantification of coupling between relative permeabilities for 2-phase flows in porous-media," Transp. Porous Media **5**, 215 (1990).
[4] K. Langaas and P. Papatzacos, "Numerical investigations of the steady state relative permeability of a simplified porous medium," Transp. Porous Media **45**, 241 (2001).
[5] N. S. Martys and H. D. Chen, "Simulation of multicomponent fluids in complex three-dimensional geometries by the lattice Boltzmann method," Phys. Rev. E **53**, 743 (1996).
[6] C. Pan, M. Hilpert, and C. T. Miller, "Lattice-Boltzmann simulation of two-phase flow in porous media," Water Resour. Res. **40**, W01501, doi: 10.1029/2003WR002120 (2004).
[7] H. Li, C. Pan, and C. T. Miller, "Pore-scale investigation of viscous coupling effects for two-phase flow in porous media," Phys. Rev. E **72**, 026705 (2005).
[8] M. Sukop, H. B. Huang, C. L. Lin, M. D. Deo, K. Oh, and J. D. Miller, "Distribution of multiphase fluids in porous media: Comparison between lattice Boltzmann modeling and micro-x-ray tomography," Phys. Rev. E **77**, 026710 (2008).
[9] T. Inamuro, T. Ogata, S. Tajima, and N. Konishi, "A lattice Boltzmann method for incompressible two-phase flows with large density differences," J. Comput. Phys. **198**, 628 (2004).
[10] X. Shan and G. Doolen, "Multicomponent lattice-Boltzmann model with interparticle interaction," J. Stat. Phys. **81**, 379 (1995).
[11] Q. J. Kang, D. X. Zhang, and S. Y. Chen, "Displacement of a two- dimensional immiscible droplet in a channel," Phys. Fluids **14**, 3203 (2002).
[12] R. Benzi, L. Biferale, M. Sbragaglia, S. Succi, and F. Toschi, "Mesoscopic modeling of a two-phase flow in the presence of boundaries: The contact angle," Phys. Rev. E **74**, 021509 (2006).
[13] H. B. Huang, D. T. Thorne, M. G. Schaap, and M. Sukop, "Proposed approximation for contact angles in Shan-and-Chen-type multicomponent multiphase lattice Boltzmann models," Phys. Rev. E **76**, 066701 (2007).
[14] P. Raiskinmaki, A. Koponen, J. Merikoski, and J. Timonen, "Spreading dynamics of three-dimensional droplets by the lattice Boltzmann method," Comput. Mater. Sci. **18**, 7 (2000).
[15] M. Latva-Kokko and D. H. Rothman, "Static contact angle in lattice Boltzmann models of immiscible fluids," Phys. Rev. E **72**, 046701 (2005).
[16] K. Sankaranarayanan, X. Shan, I. G. Kevrekidis, and S. Sundaresan, "Analysis of drag and virtual mass forces in bubbly suspensions using an implicit formulation of the lattice Boltzmann method," J. Fluid Mech. **452**, 61 (2002).
[17] A. K. Gunstensen, D. H. Rothman, S. Zaleski, and G. Zanetti, "Lattice Boltzmann model of immiscible fluids," Phys. Rev. A **43**, 4320 (1991).
[18] D. H. Rothman and J. M. Keller, "Immiscible cellular- automaton fluids," J. Stat. Phys. **52**, 1119 (1988).
[19] X. Shan and H. Chen, "Lattice Boltzmann model for simulating flows with multiple phases and components," Phys. Rev. E **47**, 1815 (1993).
[20] M. R. Swift, W. R. Osborn, and J. M. Yeomans, "Lattice Boltzmann simulation of nonideal fluids," Phys. Rev. Lett. **75**, 830 (1995).
[21] X. Y. He, S. Y. Chen, and R. Y. Zhang, "A lattice Boltzmann scheme for incompressible multiphase flow and its application in simulation of Rayleigh-Taylor instability," J. Comput. Phys. **152**, 642 (1999).
[22] T. Lee and C. L. Lin, "A stable discretization of the lattice Boltzmann equation for simulation of incompressible two-phase flows at high density ratio," J. Comput. Phys. **206**, 16 (2005).
[23] P. Yuan and L. Schaefer, "Equations of state in a lattice Boltzmann model," Phys. Fluids **18**, 042101 (2006).
[24] X. Shan and H. Chen, "Simulation of nonideal gases and liquid-gas phase-transitions by the lattice Boltzmann equation," Phys. Rev. E **49**, 2941 (1994).
[25] X. Shan, "Analysis and reduction of the spurious current in a class of multiphase lattice Boltzmann models," Phys. Rev. E **73**, 047701 (2006).
[26] C. Wang, A. G. Xu, G. C. Zhang, and Y. J. Li, "Simulating liquid- vapor phase separation under shear with lattice Boltzmann method," Sci. China, Ser. G **52**, 1337 (2009).
[27] D. G. Avraam and A. C. Payatakes, "Generalized relative permeability coefficients during steady-state 2-phase flow in porous media, and correlation with the flow mechanisms," Transp. Porous Media **20**, 135 (1995).

Author complimentary copy. Redistribution subject to AIP license or copyright, see http://phf.aip.org/phf/copyright.jsp